ELSEVIER

Polymer 42 (2001) 9031–9043

polymer

www.elsevier.com/locate/polymer

Rheology and structure of isotactic polypropylene near the gel point: quiescent and shear-induced crystallization

Natalia V. Pogodina[a], Victor P. Lavrenko[b], Srivatsan Srinivas[c], H. Henning Winter[a,*]

[a]*Department of Polymer Science and Engineering & Chemical Engineering, University of Massachusetts, Amherst, MA 01003-3110, USA*
[b]*Department of Computer Science, University of Massachusetts, Amherst, MA 01003-3110, USA*
[c]*ExxonMobil Chemical, 5200 Bayway Drive, Baytown, TX 77522, USA*

Received 17 March 2001; received in revised form 26 April 2001; accepted 26 April 2001

Abstract

Crystallizing isotactic polypropylene (iPP) develops large-scale spherulites and thick threads, large enough for observation by optical microscopy, and undergoes a liquid-to-solid transition as an expression of increased connectivity of the structure. In order to relate the time scales of structural and rheological changes, we measured time-resolved small-angle light scattering (SALS) and transmittance properties in a single experimental run, which then was repeated in an optical microscope for direct observation of growth of large-scale structures, and in a rheometer for mechanical spectroscopy. The results for quiescent and shear-enhanced melt crystallization of a high molar mass iPP are presented. In quiescent crystallization, iPP nuclei are only formed in the beginning (and not in later stages) and grow simultaneously at the same rate, which leads to spherulites of equal size. The critical gel point is reached close to the instant of the maximum of density fluctuations, but before spherulites impinge. Crystallinity estimates from H_v SALS (estimation method of Stein) are much higher than values from DSC. The discrepancy may be caused (in addition to the simplifying assumptions in the estimate) by the enhanced crystallization in the rheo-optical cell due to surface and sample loading effects. Shear flow induces anisotropic molecular conformations, preferably in the high molecular weight component of the iPP sample. The resulting orientation fluctuations (of highly oriented long chains and less oriented short chains) cause (1) an increase in nucleation rate, (2) possibly an increase in crystallization rate and (3) formation of highly elongated structures (threads) which are visible in the optical microscope and in anisotropic SALS patterns. The threads thicken until, at later stages, additional spherulites start to grow, presumably from the shorter chains and nucleated on by the threads.

Keywords: Crystallization; Gelation; Shear flow

1. Introduction

The study of polymer melt crystallization stimulated by flow has drawn much interest because it implies the possibility of controlling the final morphologies and properties of semi-crystalline polymers. By tuning the processing conditions (temperature, strain) and molecular composition, the wide range of possible molecular morphologies, such as spherulitic, shish–kebab, or row-nucleated structures, can be altered in desired ways. Flow-induced orientation and structure formation in elongational flows were thoroughly studied by Keller and co-workers [1]. Even for quiescent crystallization, the mechanism of crystal growth from the melt has become a subject of increased attention [2–4]. More experiments are needed to support further development of theory.

Isotactic polypropylene (iPP) is a useful polymer for these studies because of its large-scale, semi-crystalline structure, which not only causes a connectivity transition as measured in rheology [5,6] but also can be seen with optical experiments such as small-angle light scattering (SALS) [7], optical microscopy [8–11], and transmission intensity [12–20]. An attempt needs to be made to compare the time scales of these observations in order to merge them into a unified framework. For this purpose, we built a rheo-optical device which, in combination with an optical microscope, allows measurement of the above functions during early stages of crystallization.

Various rheo-optical methods have been used to study shear-induced orientation phenomena and structure changes in polymeric solids [21] and fluids [22,23]. Hashimoto et al. [24], Läuger and Gronski [25] and Schmidt [26] integrated SALS into a rotational rheometer. Their rheo-SALS systems are suited for simultaneous fast measurements of 2D SALS and rheological properties of polymer melts. Higgins and

* Corresponding author. Tel.: +1-413-545-0922; fax: +1-413-545-1647.
E-mail address: winter@ecs.umass.edu (H.H. Winter).

0032-3861/01/$ - see front matter
PII: S0032-3861(01)00402-5

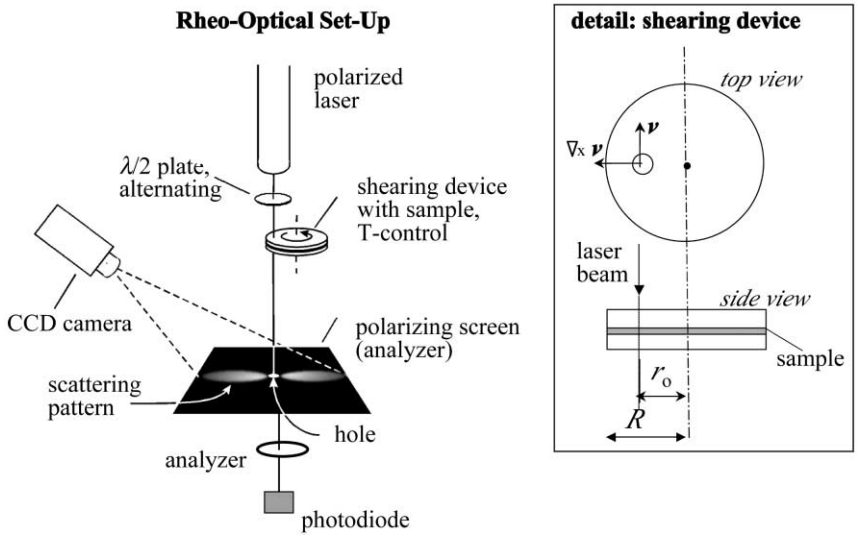

Fig. 1. Rheo-optical set-up for SALS, turbidity and birefringence measurement. Geometry of rheo-optical shearing cell.

co-workers [27] built a rheo-optical apparatus for investigating the structure of polymeric fluids under Poiseuille flow using small-angle neutron and light scattering. Important features of the design include low sample volumes and high shear-rates at the wall. Pioneering studies of shear-enhanced crystallization of polymer melts at Linz, headed by Janeschitz-Kriegl [12–16], used inhomogeneous capillary flow with parabolic velocity profile and high shear rates at the wall. Crystallization kinetics and structure development were followed by monitoring the optical retardation and turbidity. The growth of birefringence during and after short-term shear was explained by the formation of linear precursors. The shear-induced molecular orientation was assumed to be the driving force for accelerated crystallization. Due to strong shear rate and temperature gradients (shear and cooling rates were much higher in the wall layer as compared to central layer), the structure distribution in crystallized iPP reveals three distinct regions: skin-oriented layer, intermediate fine-grained layer, and spherulitic core in the center. Kornfield and co-workers [17–20] extended these experiments (short-term shearing, slit flow, high level of wall shear stress) by combining polarimetry with synchrotron X-ray scattering. They monitored the optical response of supercooled iPP melts at different temperatures upon start-up of flow and found that the time of upturn of the birefringence correlates with the rheological shift factor of the polymer melt.

The main goal of this paper is to compare the time scales of the optical, rheological and morphological changes during quiescent and shear-induced crystallization of iPP starting from the melt. In addition to dynamic mechanical spectroscopy, we report direct microscopical observation of growing thread-like structure in conjunction with time-resolved simultaneous measurements of scattered and transmitted light. A new rheo-optical device was built for this purpose and is described in this paper (Fig. 1).

2. Experimental

2.1. Materials

iPP homopolymer was chosen for this study since, below its nominal melting temperature of $T_m = 163°C$, it forms large, semi-crystalline structures which are visible in the optical microscope. Quiescent crystallization was performed on a Ziegler–Natta iPP of Fina ($M_w = 351 \times 10^3$, $M_w/M_n = 4.0$) which had been studied previously [6,7], and shear-induced crystallization was studied with a very similar iPP ($M_w = 369 \times 10^3$, $M_w/M_n = 4.0$) supplied by ExxonMobil. Polymer films (thickness 0.4 mm, diameter 20 mm) were prepared by vacuum molding at $T = 200°C$ for 10 min and subsequent cooling.

2.2. Techniques

Small amplitude oscillatory shear (SAOS) behavior was measured in a rotational rheometer (Stresstech of ATS Rheosystems) with parallel plate fixtures of 25 mm in diameter. Microscopy was studied on a Universal Polarizing Microscope (Carl Zeiss, model ZPU01). A new device was built for the rheo-optical studies. Microscope and rheo-optical device were equipped with a Linkam shearing hotstage (CSS 450 of Linkam Scientific Instruments, UK).

Temperature calibration is crucial when comparing different crystallization experiments, since crystallization kinetics is strongly dependent on undercooling. T-sensors of Linkam hotstage and rheometers were calibrated with a standard material (indium) with sharp melting point of $T_m = 156.6°C$. A thin layer of indium (0.1 mm thickness) was placed between the two parallel plates of the rheometer or of the Linkam hotstage. The sample was then heated from 150 to 170°C with constant low heating rate 1 K/min. In the rheometer, the indium melting point was detected at the

instant when the normal force applied to the sample dropped to zero. In the Linkam hotstage, the melting point was determined in the polarizing microscope as the instant when the sharp edge of the solid indium becomes diffused under melting.

In the newly built rheo-optical device (Fig. 1), linearly polarized light from a 10 mW He–Ne laser (wavelength 632.8 nm) passes through a half-wave plate (first order red) and through the shearing device which contains the polymer sample (thickness h). Scattered light from the polymer sample is captured by a polarizing screen and CCD camera (Panasonic, WV-BP310) as the detector. H_v and V_v patterns were recorded, digitized, and analyzed during the experiment. The patterns were corrected for distortions of the image arising from the angle and distance of the camera [23]. The transmitted light passes through the center hole in the screen, through a second polarizer, and onto a photodiode for intensity recording, using high-precision 6B11 and 6B12 data acquisition modules (Analog Devices).

Rotating polarizing elements are well established for the measurement of optical retardation [12–16,28,29]. Here, the polarization direction is changed by the rotation of a half-wave plate, driven by a motor equipped with encoder and controller (Micro Mo Electronics, MVP-2001 B01). Rotation of a half-wave plate (angular velocity $\omega_{\lambda/2}$ between two stationary polarizers modulates the intensity of transmitted light

$$I = \frac{I_0}{8}(1 - \cos 4\omega_{\lambda/2}t) \quad (1)$$

with quadrupled frequency $4\omega_{\lambda/2}$. The transmitted intensity, measured as photo-voltage, reaches its maximum at parallel polarization mode and minimum at crossed. I_0 is the intensity of the incident beam. A test run with one full rotation of the half-wave plate without sample provided motor positions (and half-wave plate positions) for parallel and crossed polars. These positions were then available for the actual experiment where the half-wave plate alternated between two closest positions (1/8 of a full rotation) for crossed and parallel polars. Real time measurements could thus alternate between H_v and V_v modes of SALS, birefringence and turbidity in a single experimental run. This procedure is not only convenient for data analysis but, most importantly, it increases sensitivity and reproducibility for experiments with fast transient processes. Images of scattered intensities as well as transmitted intensities in both polarization modes can be taken and analyzed at time intervals from several seconds up to several hours.

For time-resolved SALS during crystallization, both transmitted and scattered light intensities are sampled in H_v and V_v positions of polarizers (see caption of Fig. 2) at regular time intervals using a PC with image grabber DT-3152 (Data Translation) and a special-purpose software (Visual C++) which was written by one of the authors (VPL). The software is designed to compensate for optical

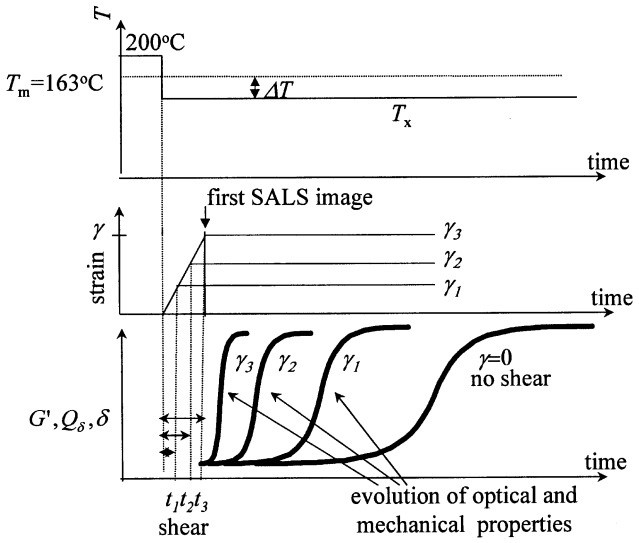

Fig. 2. Temperature protocol for shear-stimulated crystallization.

distortions [23] which are caused by the fact that the camera is not located directly above the screen but slightly offset sideways in an angle. Images can be taken as frequently as every 10 s, allowing high-resolution measurements in rapidly evolving processes. A real-time user interface updates the graphical displays on the PC screen as the data are taken. Three types of information are given on the screen: The first view shows intensity matrices of the scattered light at the most recent sampling instant as a color intensity map. The user can scroll back and forward in time, getting a visual picture of the pattern evolution. The second view shows the intensity along the azimuthal scattering angle (μ) as a function of the polar scattering angle (θ). The plot shows multiple curves (one curve per time point). Each curve can be thought of as a slice through the intensity map at azimuthal scattering angle (μ). The angle (μ) can be adjusted in a control panel, which causes displays to update immediately. The third view shows the invariants Q_δ and Q_η as a function of time, which will be defined below.

All the data gathered during an experiment get stored in internal format (for later analysis). It is possible to export the data into a text format, which can be used with popular spreadsheets and mathematical packages.

The flexible and powerful software is designed for integrated control and analysis of experiments. The experimental process is simplified by eliminating tedious manual configuration and by synchronization of components. Online data analysis provides a wealth of information while the experiment is still in progress.

In order to follow fast transient processes (i.e. dynamics of polymer melts), a special purpose software was developed which allows to collect transmitted intensity monitored by photodiode every 50 ms. The software is written in Microsoft Quickbasic. It communicates with a 6B module via serial port.

The sample was held in a Linkam shearing stage which has several advantages such as: low thermal lag, well controlled cooling/heating rates, controlled sample thickness h. Transient shear can be imposed on the sample in different modes, such as constant rate, step and oscillatory. The parallel plate geometry produces a shear field with increasing rate $\dot{\gamma}(r)$ in radial direction. However, the shear rate is constant in normal direction, which is the direction of the light beam (of light scattering). The shear was applied by the rotation of the bottom plate. The highest shear rate applied in the experiment, $\dot{\gamma} = 300\ \mathrm{s}^{-1}$, corresponds to an angular velocity

$$\Omega = \frac{v(r_0)}{r_0} = \frac{\dot{\gamma} h}{r_0} \approx 8\ \mathrm{rad/s} \tag{2}$$

Here $r_0 = 7.5$ mm is the radial position of the laser light beam passing through the sample, Ω the angular velocity of the bottom plate, $v(r_0)$ the velocity at radius r_0 of the moving plate and $h = 0.2$ mm the thickness of the sample. Inertial effects are negligible compared to viscous effects (Reynolds number does not exceed $Re \leq 5 \times 10^{-5}$). For our samples, the upper limiting shear rate was much below $\dot{\gamma} = 300\ \mathrm{s}^{-1}$, due to excessive normal stresses which would bend the Linkam device.

2.3. Temperature and shearing protocol

The shearing device was referenced beforehand to its upper position with an initial gap of $h = 2.5$ mm and the polymer sample was inserted between the glass windows of the shearing device. The polymer sample was annealed at $T = 200$°C for 3 min and then pressed slowly to its final thickness $h = 0.2$ mm by lowering the upper glass plate. After having reached the final thickness, the sample was cooled (without shearing) at maximum cooling rate (30 K/min) to a desired crystallization temperature. $T_x = 148$°C has been used in all crystallization experiments. $T_x = 190$°C has been used for comparison purposes. After isothermal conditions were reached, the sampling (data collection) started either immediately, for quiescent crystallization, or after applied 'short-term' shear with constant shear rate, for flow-induced crystallization. The time of shearing ($t \leq 60$ s) was considerably shorter than crystallization time at T_x so that crystallization during shear was minimized. After deformation up to a prescribed strain, the flow was stopped and crystallization was monitored optically by scattered and transmitted light. The temperature protocol for shear-stimulated crystallization is shown in Fig. 2.

2.4. Analysis of rheological data

In SAOS, the dynamic moduli are expressed as in-phase (G') and out-of phase (G'') components of the sinusoidal stress

$$\tau = \tau_0 \sin(\omega t + \delta) = G' \gamma_0 \sin \omega t + G'' \gamma_0 \cos \omega t \tag{3}$$

Here γ_0 is the amplitude of the imposed strain, δ the phase angle between strain and stress. The rise of G' and G'' in time during the crystallization process reflects the increasing molecular connectivity of the material. At the gel point, the low frequency dynamic moduli afford self-similar behavior [30]

$$G'_c = \frac{G''_c}{\tan \delta_c} = S_c \Gamma(1 - n_c) \cos \frac{n_c \pi}{2} \omega^{n_c} \qquad \text{for } \omega < 1/\lambda_0 \tag{4}$$

Here S_c and n_c are the gel stiffness and the relaxation exponent, Γ the gamma-function. A consequence of the self-similar dynamics (at the gel point) is a frequency-independent loss tangent

$$\tan \delta_c = \tan \frac{n_c \pi}{2} = \text{const} \qquad \text{for } \omega < 1/\lambda_0 \tag{5}$$

in the terminal zone. This frequency independence provides a most reliable and generally valid method for determining the gel time and the material parameters n_c and S_c.

In order to follow the transient relaxation behavior during gelation, the relaxation time spectrum was calculated at different instants of solidification process starting from the melt. The complex motion of polymer chains is described as a set of different relaxation modes (set of exponential decays), which constitute the relaxation modulus

$$G(t) = G_e + \sum_{i=1}^{N} g_i \, e^{-t/\lambda_i} \tag{6}$$

where N is the number of relaxation modes, λ_i the relaxation time of ith mode and g_i the strength of this ith mode. The equilibrium modulus G_e is finite for solids ($G_e > 0$) and zero for liquids ($G_e = 0$). The relaxation time spectrum was determined from experimental values of dynamic moduli by conversion from the frequency domain to the time domain using the method of Baumgaertel and Winter [32].

2.5. Analysis of SALS and birefringence data

A beam of polarized light interacts with the microstructure of the crystallizing sample and gets scattered. Scattering at small angle (SALS) gives information about large fluctuations in density and orientation. The scattered light depends on the angle between polarizer (P) and analyzer (A). If P and A are parallel (V_v and H_H), the scattering is labeled as polarized, and if they are crossed (H_v and V_H), the scattering is depolarized. The direction of the shear flow with respect to polars is also important. Different settings of P and A in rheo-SALS experiment give polarization conditions of the scattered light as specified in the figures.

There are two contributions to polarized V_v and H_H scattering, one originating from concentration and density fluctuations, i.e. on fluctuations of the isotropic part of polarizability, and the other originating from fluctuations of the anisotropy of the polarizability and orientation of the optical axis [21]. Unlike polarized scattering, the

depolarized H_v and V_H scattering depends only on the fluctuations of optical anisotropy and orientation. H_v and V_H scattering are equal if the sample does not show a strong optical rotation (which is true for the samples studied in this work). If the sample would be strongly optically active, the depolarized SALS patterns would be distorted and lose their characteristic fourfold symmetry [32,33].

Depolarized scattering is particularly important for anisotropic structures, since the scattering beam emitted by induced dipoles in the sample (in contrast to isotropic structures) is no longer polarized in the same direction as the primary beam. The induced dipole moment $\mathbf{m}(r)$ and the anisotropy $\delta_n(r)$ in anisotropic system are given by [21,34]

$$\mathbf{m}(r) = \delta_n(r)(\mathbf{a}(r)\cdot\mathbf{E})\mathbf{a}(r) + \alpha_2(r)\mathbf{E} \tag{7}$$

with

$$\delta_n(r) = \alpha_1(r) - \alpha_2(r) \tag{8}$$

where $\alpha_1(r)$ and $\alpha_2(r)$ are the principal polarizabilities parallel and perpendicular to the principal optic axis along the unit vector $\mathbf{a}(r)$. Uniaxial symmetry of polarizability is assumed.

With much calculation, the polarized and depolarized scattering intensities for simple systems may be found; thereby contributions of density and orientation fluctuations may be separated from the overall intensity [35,36].

$$I_{H_v}(q) = 4\pi\left(\frac{E_0^2\omega'^4}{r^2c^4}\right)V\sin^2\psi\langle\delta_n^2\rangle\frac{1}{15}\int_0^\infty f(r)\frac{\sin(qr)}{qr}r^2\,\mathrm{d}r \tag{9}$$

$$I_{V_v}(q) = 4\pi\left(\frac{E_0^2\omega'^4}{r^2c^4}\right)V\sin^2\psi\left[\langle\eta^2\rangle\int_0^\infty\gamma(r)\frac{\sin(qr)}{qr}r^2\,\mathrm{d}r + \frac{4}{45}\langle\delta_n^2\rangle\int_0^\infty f(r)\frac{\sin(qr)}{qr}r^2\,\mathrm{d}r\right] \tag{10}$$

$$I_{V_v}(q) - \frac{4}{3}I_{H_v}(q) = 4\pi\left(\frac{E_0^2\omega'^4}{r^2c^4}\right)V\sin^2\psi\langle\eta^2\rangle\int_0^\infty\gamma(r)\frac{\sin(qr)}{qr}r^2\,\mathrm{d}r \tag{11}$$

where ψ is the angle between the dipole $\mathbf{m}$ and the vector $\mathbf{r}$ extending from the dipole to the observer, V the volume of the scattering system, ω' and E_0 the angular frequency of the electromagnetic wave and the amplitude of the primary electrical field strength, respectively, c the speed of light in vacuum, $q = (4\pi/\lambda)\sin(\theta/2)$ the scattering vector, $\lambda = 632.8$ nm is the wavelength of the laser light, θ and μ the polar and azimuthal scattering angles. $\langle\eta^2\rangle$ is the mean-square density fluctuation, and $\langle\delta_n^2\rangle$ is the mean-square orientation fluctuation. $f(r) = [3\langle\cos^2\theta_{ij}\rangle_r - 1]/2$ is the correlation function of orientation fluctuation, where θ_{ij} is the angle between optic axes of the i and j volume elements separated by a distance r. $\gamma(r) = \langle\eta_i\eta_j\rangle/\langle\eta^2\rangle$ is the correlation function of the density fluctuation, where $\eta_j = \alpha_j - \langle\alpha\rangle$ is the polarizability fluctuation at position j. In our experiments, we used two polarization modes V_v and H_v. For the system under investigation, the V_H mode can be used instead of H_v since depolarized intensities are equal. However, using the H_H mode instead of the V_v mode for our optically anisotropic system will decrease the polarized intensity, since the shear flow is in V-direction and molecules orient preferentially in the vorticity plane.

It should be pointed out that the Stein–Wilson theory (briefly summarized above) predicts scattering that is circular about the incident beam (independent of azimuthal angle μ). This is a consequence of an assumption implicit in its derivation of 'random orientation correlations'. A more general treatment [37] leads to azimuthally dependent scattering.

Crystallization kinetics can be conveniently described in terms of the invariants Q_δ and Q_η which are defined as integrated scattering intensities [38] along a line (i.e. along scattering vector)

$$Q_\delta = \int I_{H_v}q^2\,\mathrm{d}q = \frac{2\pi^2}{15}\left(\frac{\omega}{c}\right)^4\langle\delta_n^2\rangle \tag{12}$$

$$Q_\eta = \int\left(I_{V_v} - \frac{4}{3}I_{H_v}\right)q^2\,\mathrm{d}q = 2\pi^2\left(\frac{\omega}{c}\right)^4\langle\eta^2\rangle$$

In effect, the imaging software is calculating the sums $(1/N_p)\sum_{k=1}^{N_p} I_k q_{ki}^2$, where N_p is the number of pixels along a line (1D invariant) or of the entire area (2D invariant) and I_k the intensity above the initial intensity level (before crystallization). Hence, from the temporal evolution of the invariants, the crystallization kinetics can be probed in terms of density and orientation fluctuations.

Thus, Q_η parallels the growth of mean-square density fluctuations $\langle\eta^2\rangle$ and Q_δ parallels orientation fluctuations, i.e. mean-square optical anisotropy $\langle\delta_n^2\rangle$. The Q_δ-invariant can also be expressed in terms of structural, optical, and crystalline parameters of growing spherulites [39].

$$Q_\delta = \frac{K}{15}\langle\delta_n^2\rangle = \phi_{sp}[\delta^0_{n\,cr}X_{cr,s}f + (\alpha_r - \alpha_t)_{am}]^2 \tag{13}$$

Here $X_{cr,s}$ is the volume fraction crystallinity within the spherulite, f the Hermans orientation function of the crystals with respect to the radius of the spherulite, $\delta^0_{n\,cr}$ the intrinsic anisotropy of a pure crystal, $(\alpha_r - \alpha_t)_{am}$ the amorphous contribution to spherulite polarization, α_r and α_t the radial and tangential polarizabilities, respectively, ϕ_{sp} the volume fraction of spherulites. When $\phi_{sp} = 1$, spherulites become volume filling. K is the product of physical constants. Real time computation of one- and two-dimensional integrals allows graphing of time dependent scattered intensities and invariants during the experiment.

Additional information is gained from the transmitted

light. The appearance of inhomogeneities (growing crystals) affects the transmittance of polarized light in two ways: turbidity arises from the loss of intensity due to scattering from optically heterogeneous clusters, and birefringence in crossed polars arises from anisotropic clusters.

For perfectly oriented molecules, the difference between the refractive indices in two principal directions, birefringence $n_e - n_0$, may be related to the polarizability difference $\alpha_1 - \alpha_2$ to give [21,36]

$$\Delta = n_e - n_0 = \frac{2}{9}\pi\left[\frac{(n^2+2)^2}{n}\right]N(\alpha_1 - \alpha_2) \tag{14}$$

where $n = (n_1 + n_2 + n_3)/3$ is the average refractive index, N the number of molecules in the control volume. Thus, the birefringence is a measure of the molecular orientation and for a multi-component system (with different orientation of each optical axis) is given by

$$\Delta = \frac{2\pi}{9}\left[\frac{(n^2+2)^2}{n}\right]\sum_i [(\alpha_1 - \alpha_2)_i f_i] \tag{15}$$

Shear flow imposed on the system initiates molecular orientation in the flow direction. Therefore, the value of birefringence will be dependent on the angle between shear direction and crossed polars. For maximum retardation, the molecular axes should be oriented at 45° to the polarization directions. Birefringence is determined from transmitted intensities I_+ and $I_\parallel$ in crossed and parallel polars, respectively. The optical phase difference (optical retardation) is given by [12,14,52]

$$\delta'_n = \frac{2\pi h}{\lambda}(n_1 - n_2) = 2\arcsin\left(\frac{I_+}{I_+ + I_\parallel}\right)^{1/2} \tag{16}$$

$n_1 - n_2$ is the optical birefringence of the material (difference between two refractive indices, n_1 and n_2, where n_1 is parallel to the flow and n_2 is perpendicular). Eq. (16) implies that the optical axis of the sample is oriented at 45° with P. Eq. (16) holds with the assumption that losses in transmitted light due to scattering and absorption can be neglected. For crystallizing polymers as studied here, the experiment gives only qualitative information of the time scale of the ordering process and not the quantitative value of the optical retardation.

The transmitted intensity in parallel polars $I_\parallel$ defines the turbidity τ of the sample:

$$\frac{I_\parallel}{I_0} = e^{-\tau h}, \qquad \tau = -\frac{1}{h}\ln\frac{I_\parallel}{I_0} \tag{17}$$

where I_0 is the intensity transmitted without sample and h the sample thickness. The loss of transmitted intensity results from scattering and from absorption in the sample.

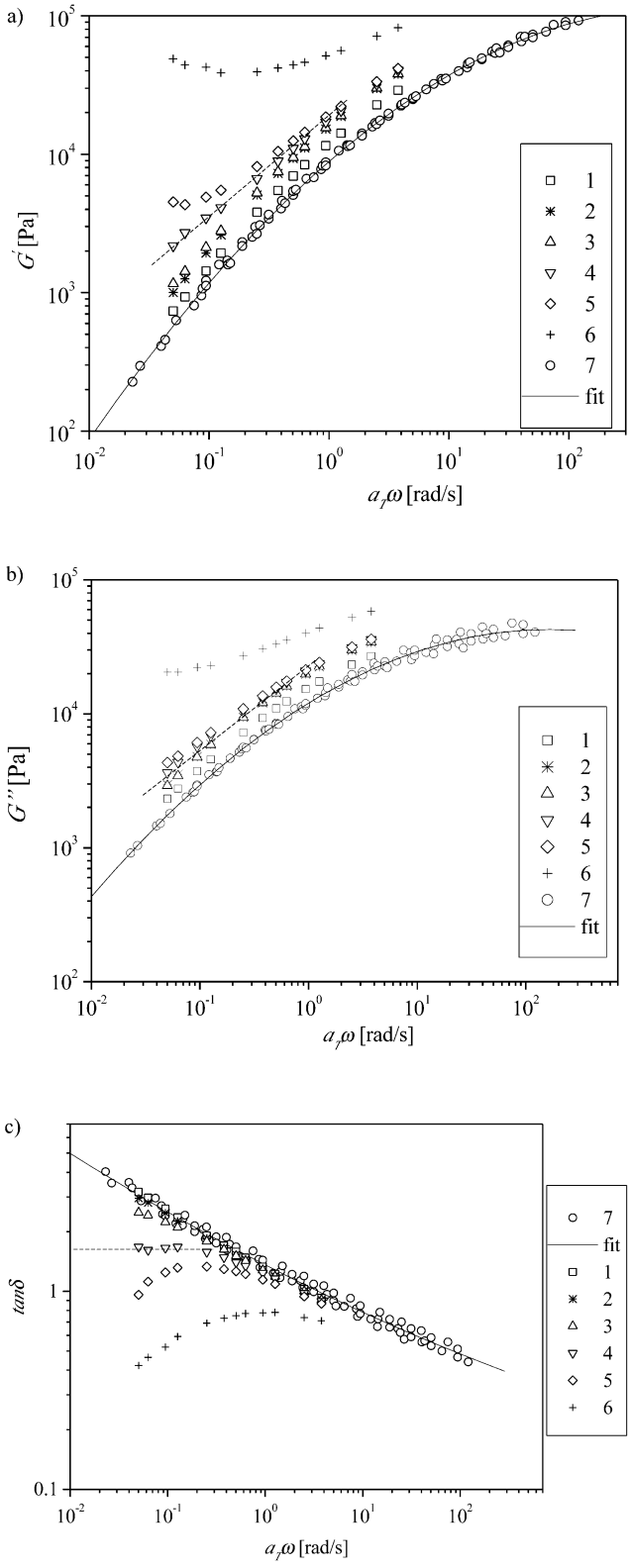

Fig. 3. Evolution of (a) storage moduli, (b) loss moduli and (c) tan δ at different instants during crystallization at $T_x = 148$°C: 1.175 (1); 15 (2); 20 (3); 22 (4); 25 (5); 79.5 (6) ($\times 10^3$ s); mastercurve for melt (7) shifted to $T_{ref} = 148$°C. The solid line through the data points on the mastercurve is calculated with the fitted relaxation time spectrum [31]. The gel point is marked by a dashed line.

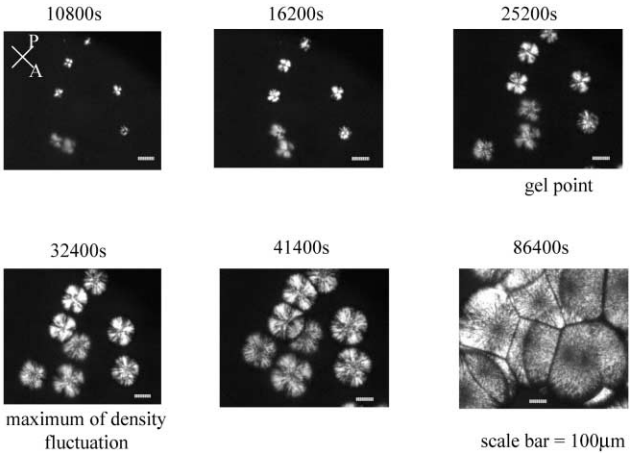

Fig. 4. Spherulites observed in polarizing microscope during quiescent crystallization at the same sequential instants as in SALS ($T_x = 148$°C). Scale = 100 μm. Some spherulites are not in focus due to their different distances from the objective (sample thickness was 200 μm).

3. Experimental results and discussion

3.1. Quiescent crystallization and morphology development of iPP

Fig. 3a–c shows the evolution of storage modulus, loss modulus and tan δ as a function of $a_T\omega$ at increasing crystallization times at $T_x = 148$°C, starting from the melt. The curve with open circles belongs to the mastercurve of the melt, shifted to $T_{ref} = 148$°C. Within the accessible frequency range, $G'(a_T\omega)$ and $G''(a_T\omega)$ in Fig. 3a and b do not reach the typical low frequency asymptotes of slopes 2 and 1. This broad crossover to the terminal zone is the expression of a broad molecular weight distribution of the iPP. As the crystallization proceeds, the slopes of G' and G'' at lower frequencies decrease from 1.2 and 0.8, respectively, in the melt to about $n_c = 0.65$ near the gel point. In the low frequency region, the slope of tan $\delta(a_T\omega)$ in Fig. 3c changes from negative at early times in the melt to positive at fully crystallized solid state. The gel point is identified by tan δ becoming independent of frequency (curve 4 in Fig. 3c). The estimated gel time (with the accuracy of the time length of one frequency sweep in SAOS) is $t_c = (22 \pm 3) \times 10^3$ s. The gel point value, tan $\delta_c = 1.62$ gives $n_c = 2\delta/\pi = 0.647$ which confirms the n_c-value determined from $G'(\omega)$, $G''(\omega)$ slopes. A limitation of the experiments shows at the very low frequencies where the crystallization rate is too high for the long experimental time (see low frequency upturn in uppermost G'-curve, Fig. 3a).

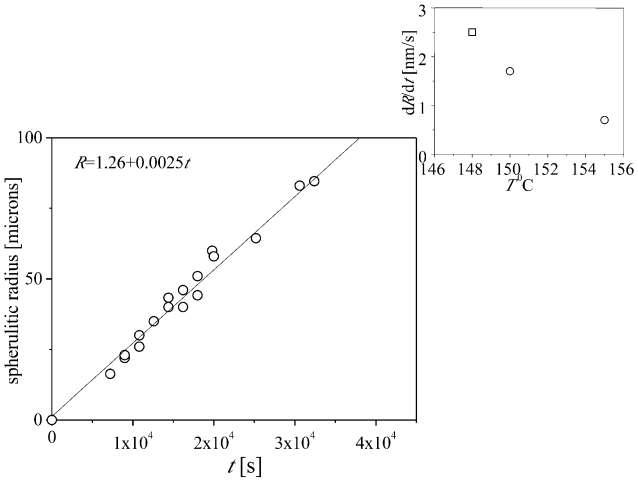

Fig. 5. The spherulite radius growth in time during quiescent crystallization of iPP at $T_x = 148$°C. The radius of growing spherulites was taken from optical micrographs at increased magnification 40×. The average of four independent runs shows reasonable reproducibility. In the upper right corner: the growth rate of the spherulite dR/dt versus crystallization temperature (circles: data of Olley and Bassett [40], square: present data).

Spherulite growth during quiescent crystallization of iPP can be observed directly in optical micrographs (Fig. 4) together with the corresponding SALS patterns (Fig. 6). Semi-crystalline spherulites nucleate at about the same time and grow at the same rate of about dR/d$t = 2.5$ nm/s, Fig. 5, until they impinge with each other. This growth rate agrees with data of Olley and Bassett [40] for the same crystallization temperature range and a similar iPP (see inset of Fig. 5). SALS patterns develop fourfold symmetry at later times that confirms the growth of crystallinity in the anisotropic spherulites.

SALS invariants Q_η and Q_δ, calculated from data of Fig. 6, are an expression of the growing fluctuations of density and orientation, see Fig. 7. Density fluctuations appear at the very early times, pass through a maximum and decrease at later stages of crystallization when the crystalline phase becomes dominant [7,46]. The orientation fluctuations due to optically anisotropy of crystals develops at much later stages and shows sigmoidal growth. This is the typical SALS pattern of spherulitic growth in quiescent crystallization of iPP [7,46].

The SALS invariant Q_δ grows at the same rate as the storage modulus G' (here at $\omega = 0.05$ rad/s), see Fig. 8.

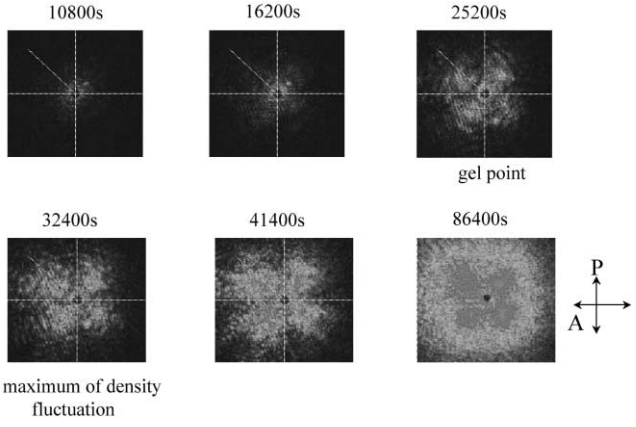

Fig. 6. SALS images in crossed polarizers observed at different sequential instants during quiescent crystallization of iPP ($T_x = 148$°C). Same times as in Fig. 4.

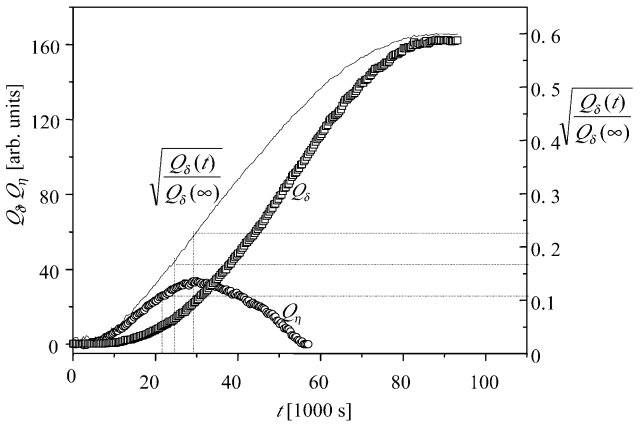

Fig. 7. Time variation of Q_η and Q_δ and estimate of absolute crystallinity $X(t) \propto \sqrt{Q_\delta(t)/Q_\delta(\infty)}$. Crystallinity at the gel point and at spherulitic impingement is shown by the lines.

This means that solidification parallels the development of mean-square optical anisotropy during crystallization. As a simple order of magnitude estimate of gel-times, we take the time at which the modulus has grown to 10% of is final value [41]. For a final value of $G'_{\max} \approx 5 \times 10^4$ Pa at late crystallization stage (see Fig. 8), 10% will give $G' \approx 5 \times 10^3$ Pa. The corresponding gel time estimate is $t_c = 25 \times 10^3$ s.

An attempt to monitor the DSC data at the actual crystallization temperature $T_x = 148$°C showed no detectable peak (at least up to the instant of gelation and the instant of maximum density fluctuation) $t = 30\,000$ s. In the absence of absolute measurements of crystallinity at slow crystallization (high T_x), we follow Stein's suggestion [39] and estimate the growing fraction of crystalline material as

$$X(t)_{\mathrm{SALS}} = \sqrt{\frac{Q_\delta(t)}{Q_\delta(\infty)}} \tag{18}$$

where $Q_\delta(t)$ and $Q_\delta(\infty)$ are invariants values at the instant 't' and at long crystallization times, respectively. The

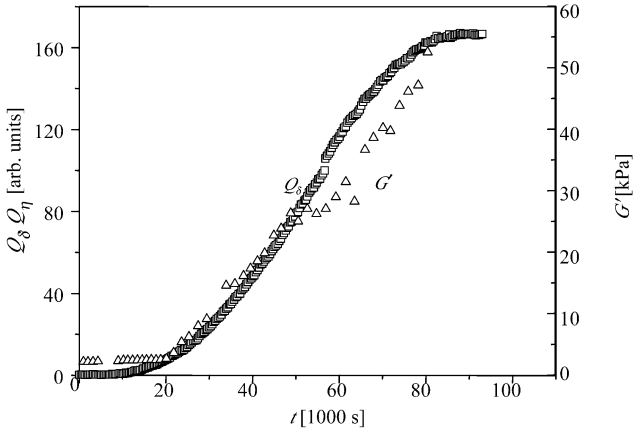

Fig. 8. Time variation of Q_δ (from SALS) and storage modulus G' at $\omega = 0.05$ rad/s (from rheology).

advantage of this method is that all measurements are performed in a single experiment so that crystallinity at the gel point can be estimated indirectly from the Q_δ invariant (Eq. (18)). The main assumptions are that spherulites are volume filling at the instant of impingement, that Hermans orientation function value (f) does not change significantly with spherulitic impingement and amorphous spherulite polarization $(\alpha_r - \alpha_t)_{am}$ at $T_x = 148$°C is negligible. The absolute crystallinity is then estimated as $X(t)_{abs} \approx 0.6X(t)_{SALS}$ since the maximum attainable crystallinity in fully crystallized iPP samples is about 60%. The estimated values are $X_{gel} = 12$–17% at the gel point, and $X_{\eta\,max} = 24\%$ at the maximum of density fluctuations. The growth of $0.6\sqrt{Q_\delta(t)/Q_\delta(\infty)}$ is plotted in Fig. 7.

It needs to be mentioned that the estimated value of absolute crystallinity for iPP critical gels is about 5–6 times higher than the one presented in our previous publications [5–7]. The discrepancy may be caused by the different methods used for the determination of crystallinity. Also, in Refs. [5–7], the crystallinity at the gel point was estimated by extrapolation from DSC data of samples, which were crystallized at relatively low temperatures, $T_x = 123$–136°C (crystallization rate constants were extrapolated for the extended higher T_x). The Avrami crystallization exponent N_A was set to $N_A = 2.5$. The difference could also be caused by real differences in the crystallization process, for instance, due to differences in surfaces of the rheo-optical cell as compared to the sample holder of DSC. This difference in crystallinity values from different methods needs further experimental study.

After comparing rheological, scattering and microscopical data, we identified four trends in early stages of quiescent crystallization of iPP:

- The structure development can be observed microscopically before the gel point is reached.
- Growing structures (in quiescent crystallization) become visible simultaneously as spherulites of about equal diameter.
- The image corresponding to the critical gel state (gel time $t_c \approx 22\,000$–$25\,000$ s) is shown in the upper right corner of Fig. 4. The critical gel consists of visible spherulites (semi-crystalline phase) surrounded by an amorphous matrix phase. Spherulites do not yet touch but they interconnect through the melt, which provides tie chains between spherulites to form the network.
- The maximum of density fluctuation from SALS data (Fig. 7) occurs at $t_{Q_\eta\,max} = 30 \times 10^3$ s. The corresponding microscopic image is presented in the lower left corner in Fig. 4 and shows large spherulites which will impinge soon. Thus, the maximum density fluctuations occur close to the instant of spherulitic impingement, which confirms the result of Ref. [39].

According to Horst and Winter [42], two types of connectivity are possible in crystallizing polymer systems. In the

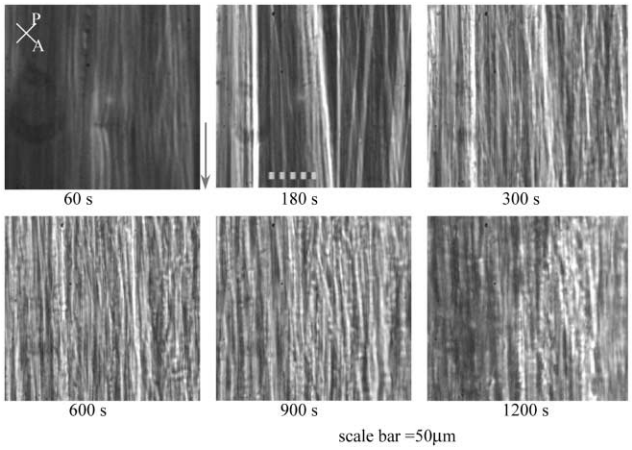

Fig. 9. Microscopic images taken at different times during shear-induced crystallization of high molecular iPP $M_w = 3.5 \times 10^5$, $T_x = 148°C$, $\dot{\gamma} = 10\ s^{-1}$, $t = 60$ s, $\gamma = 600$.

first type, crystals act as effective crosslinks, which connect macromolecules into a network gel. In the second type, large semi-crystalline structures (spherulites, cylindrites, etc.) are formed and interconnect through amorphous tie-chains. In terms of this approach, the iPP-gel belongs somewhere in between, possibly closer to the second type.

3.2. Shear-induced crystallization and morphology development

3.2.1. Simultaneous scattering and transmittance data

Morphological changes during shear-induced crystallization were followed by time-resolved optical studies and are presented as micrographs (Fig. 9) and SALS images (Fig. 10). All data are taken by shearing the iPP for 60 s and then stopping the flow. The formation of threads is directly followed microscopically during and after cessation of shear flow in undercooled melt samples (Fig. 9). The first image is taken at the instant of flow cessation (after 60 s of imposed shear). The semi-crystalline threads are just beginning to be formed and can be viewed on the dark field of residual amorphous melt. Threads grow oriented parallel to the flow direction. The threads grow in thickness until, at much later times, additional spherulites start to grow. Threads are found only for high-molecular weight iPP after continuous shear for 60 s and at a relatively high shear rate of $10\ s^{-1}$. This indicates that critical shear rate and shearing time, i.e. total strain is needed to be imposed on the system in order to initiate linear superstructures. This might be the reason why for shear-induced crystallization at lower shear rates (below $1\ s^{-1}$), only multiple continuous nucleation is reported while maintaining the same type of spherulitic morphology, typical for quiescent crystallization [8–11].

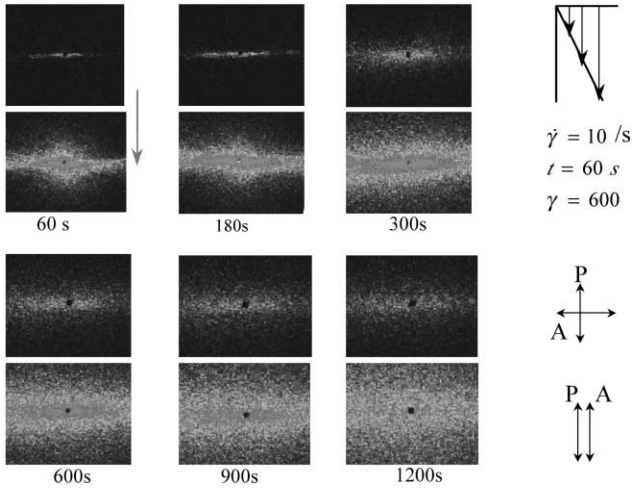

Fig. 10. H_v and V_v images during shear-stimulated crystallization of iPP, $M_w = 3.5 \times 10^5$, $T_x = 148°C$. Shearing conditions: $\dot{\gamma} = 10\ s^{-1}$, $t = 60$ s, $\gamma = 600$. Flow is parallel to polarization direction.

Fig. 10 shows the corresponding H_v and V_v SALS images. The arrow indicates the direction of the flow. For flow parallel to the polarization direction (Fig. 10), strong streaks develop at early stages of crystallization. The SALS streaks orient perpendicular to the flow direction. In V_v mode, streaks are more pronounced due to higher scattering intensity. Strong streaks mean that the intensity of scattered light is highly anisotropic and is much stronger in the perpendicular than in the parallel direction with respect to the flow. This indicates that actual scatterers (due to Fourier transform procedure) are oriented along the flow direction (or at least in the vorticity plane). Preferential orientation of scatterers along the flow direction is the consequence of elongated structures (threads) formed by the flow. At later times, images in Fig. 10 show a tendency to a circularly symmetric pattern. This means that growing morphologies tend to randomization in space. In micrographs (Fig. 9), randomization of growing morphologies is seen as spherulitic overgrowth at later times (last three sequential micrographs in Fig. 9). At very late stages, 5–10 h after flow cessation, the micrographs show only impinged spherulites, grown over threads.

Two-dimensional invariants of scatttered light in both modes are shown in Fig. 11. Density fluctuations are seen to grow quickly from the start and pass through a maximum. Orientation fluctuations show sigmoidal growth and reach saturation at about the time when density fluctuations pass through a maximum ($t \sim 900$ s). This indicates that due to orientational and deformational effects of shear flow, the system of solidifying clusters (threads) reaches rapidly the state of the final crystallinity, attainable for this sample in this shear-enhanced process. We found that in quiescent crystallization, the liquid–solid transition occurs close to the instant of the maximum of density fluctuations in the system, i.e. to the instant of spherulitic impingement. We may speculate that the same trend is true for shear-induced crystallization, i.e. the instant of the maximum of density fluctuation ($t = 900$ s in Fig. 11) is in the vicinity of the gel point. This allows to visualize transient gel in shear-enhanced crystallization as the network with thread-like structure shown on the micrograph at $t = 900$ s in Fig. 9.

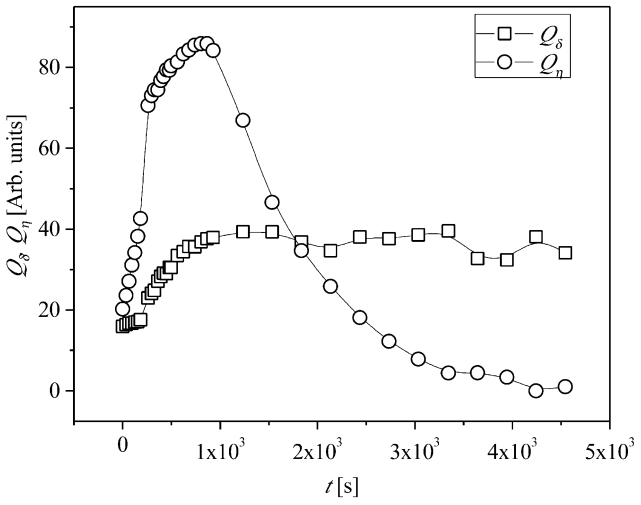

Fig. 11. Time variation of Q_η and Q_δ during shear-stimulated crystallization of iPP. Two-dimensional integration over the entire area (2D invariant). Shearing conditions: $\dot{\gamma} = 10\ s^{-1}$, $t = 60$ s, $\gamma = 600$. Flow is parallel to polarization direction.

Fig. 12 shows the growth of optical phase difference and turbidity in shear-stimulated crystallization estimated according to Eqs. (16) and (17). The simultaneous increase of δ'_n and τ suggests that optical heterogeneity (sensed as turbidity in parallel polars) and optical anisotropy of oriented threads (sensed as optical retardation in crossed polars) grow simultaneously. This greatly differs from the quiescent case where optical heterogeneity (density fluctuations) evolves much faster than optical anisotropy (orientation fluctuations). The value of the optical phase difference at its saturation $\delta_{n\ \max}$ (Fig. 12) can be used to estimate the birefringence of fully crystallized iPP samples, which is an important structural characteristic of the material after processing:

$$\Delta n = \frac{\delta'_{n\ \max}\lambda}{2\pi h} = \frac{1.5 \times 0.6328\ \mu m}{6.28 \times 200\ \mu m} = 7 \times 10^{-4} \qquad (19)$$

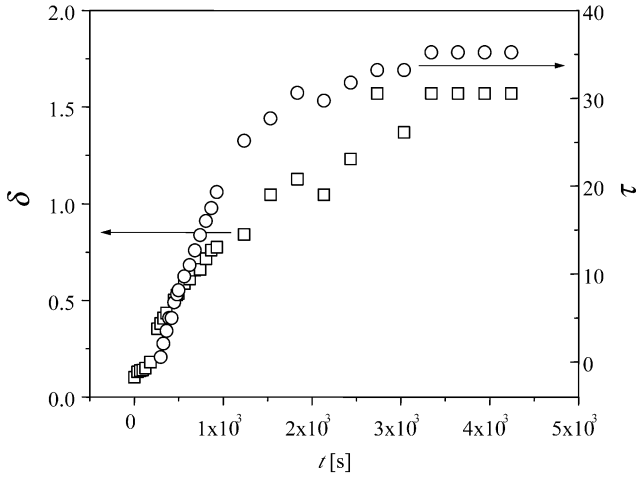

Fig. 12. Growth of the optical retardation δ (left axes) and turbidity τ (right axes) during shear-induced crystallization at 148°C and $\gamma = 600$.

The value of birefringence is rather small. So it is reasonable to assume that except oriented thread-like morphologies there are chain-folded morphologies. The combination of both morphological types gives rise to the so-called 'crossed' local orientation characterized by the low optical anisotropy.

3.2.2. Transmittance measurement in fast mode

To understand better, we complemented our time-resolved microscopy of evolving threads with the studies of chain melt dynamics. We studied iPP chain melt rheology in the temperature range $T = 210$–140°C as well as the dynamic response of iPP melt under imposed flow and after flow cessation at two temperatures $T = 190$ and 148°C.

The dynamic response of iPP melt was studied by monitoring the change in transmitted intensity in crossed polars I_+ during flow and after flow cessation at two different temperatures and preshear history: $T = 190$°C, $\dot{\gamma} = 10\ s^{-1}$, $t = 100$ s, $\gamma = 1000$ and $T_x = 148$°C, $\dot{\gamma} = 10\ s^{-1}$, $t = 60$ s, $\gamma = 600$. Shear was applied for a longer time $t = 100$ s at $T = 190$°C to gain higher total strain for low-viscous iPP melt. Raw data without filtering are presented in Fig. 13. At both temperatures, the increase in I_+ is observed after flow cessation, that indicates formation of anisotropic structures. The physical origin of the arising anisotropy comes from orientation, extension and coalescence of macromolecules caused by the shear flow. However, at $T = 190$°C (which is higher than nominal melting temperature $T_m = 163$°C determined from DSC peak), the oriented structures relax after 3–4 s (see inset in Fig. 13). At $T_x = 148$°C (Fig. 13), oriented and stretched chains do not relax for much longer time. The continuous growth of I_+ at $T_x = 148$°C in Fig. 13 means that more and more macromolecules join the oriented state. Comparison of raw data in shearing experiments at two different temperatures (Fig. 13) shows that at $T = 190$°C orientation and relaxation of iPP chains takes place (molecular dynamics), while at $T_x = 148$°C orientation of iPP chains is followed by the formation of supermolecular linear precursors from non-relaxed adjacent chains.

3.3. Molecular origin of thread-like morphologies

The formation of linear precursors was proposed for interpretation of different dynamically induced crystallization processes, such as crosslinked oriented (stretched) polyethylene [43], flow-induced crystallization in capillary [12–16,20,44,45] and extensional flows [1]. It is now accepted that linear precursors lead to the formation of 'shish–kebabs', which were observed in pioneering studies of Pennings [47–49] and extensively studied by Keller [1].

Shish–kebabs are crystalline assemblies consisting of two components: a central core fiber (the 'shish') and lamellae (the 'kebabs') strung along this core. Flow of the appropriate kind and strength will extend/orient the long

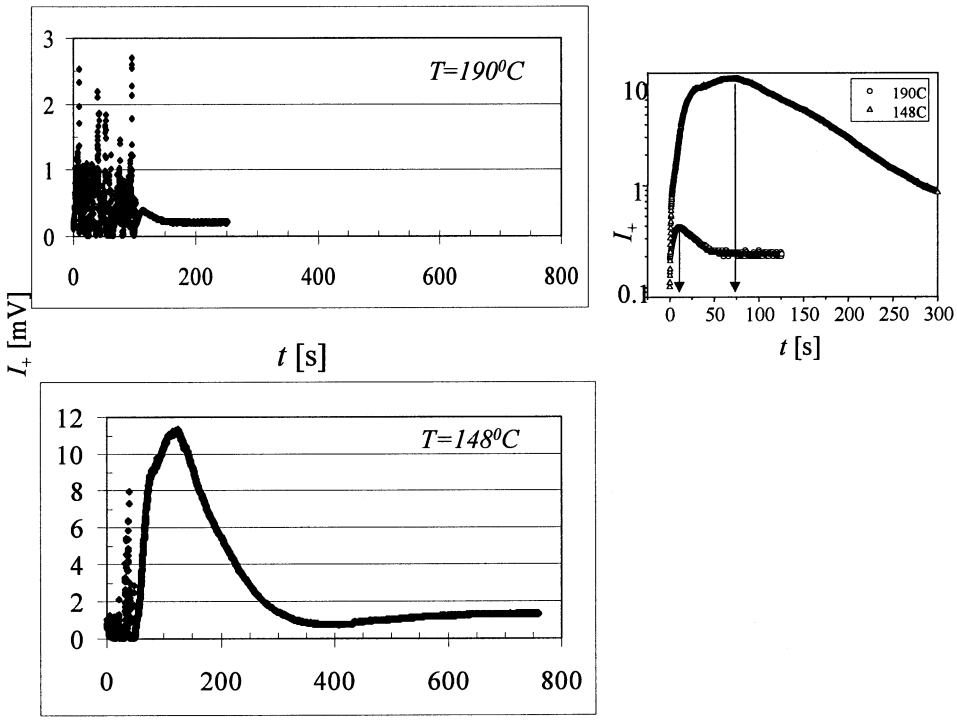

Fig. 13. Transmitted intensity in crossed polars I_+ versus time during and after flow cessation for polymer melt at two different temperatures $T_x = 148°C$, $\dot{\gamma} = 10\ s^{-1}$, $t = 10$ s, $\gamma = 600$ (right axes) and $T = 190°C$, $\dot{\gamma} = 10\ s^{-1}$, $t = 10$ s, $\gamma = 600$ (left axes). Monitoring starts at flow start-up. In the upper right corner, the response after flow cessation is shown in semi-logarithmic scale for clarity, the arrows indicate the instant when I_+ reaches maximum.

chains of the material giving rise to fibrous crystals aligned along the flow, with the remainder of the material crystallizing into chain-folded platelets [1]. Initially observed in solutions [47–49], shish–kebabs were later accepted as the main resultant fiber-platelet morphology in (elongational [1] and shear [12–20,45]) flow-induced melt crystallization. However, the kinetics of their formation (which originates from chain melt dynamics in the flow field) is still not clear.

The overall motion of polymer chains in the melt is governed mostly by entanglements. Physically, it was successfully described in terms of Doi-Edwards' tube-model. According to the tube-model, chain motion in the melt is constrained by an imaginary tube formed by environmental molecular chains and only reptation along the tube is permitted. The number of topological constraints (the entanglement density) is determined by temperature (Brownian motion) in the quiescent melt and additionally by the shear rate and total strain imposed in shear flow. When shear flow is applied, the entanglement density decreases because the polymer chains are pulled away and polymer chains are oriented and extended. The degree of orientation and extension of polymer chains is governed by conformational relaxation time, which is temperature and molecular weight dependent.

For linear polymers in the molten state, the longest relaxation time λ_{max} scales with weight-average molecular weight as $\lambda_{max} \propto M^{3.4}$. This has been confirmed by many experiments reported in the literature. The iPP sample is broadly distributed and the distribution of molecular sizes affects the relaxation behavior of the polymer melt. Long chains relax faster in the presence of short chains and short chains are hindered in their relaxation by the presence of long chains. The distribution of molecular sizes results in a broadened distribution of longest relaxation times for the individual molecules. Experimental times for the shear experiments can be chosen such that the long chains are oriented at onset of crystallization while a sufficient fraction of short chains have had sufficient time to relax.

At our chosen experimental conditions ($T_x = 148°C$ and constant shear for 60 s), long chains attain higher degree of orientation and alignment in the flow. These chains do not relax for the time enough to form coalescence ('bundles') of adjacent chains with lower free energy, which serve as precursors (linear nuclei) for crystallization. Important condition for coalescence of adjacent chains to be formed is continuous shearing of the remaining melt. As a result, these long adjacent chains, brought together by the flow, crystallize in the fibrillar form at temperature below melting. The shorter polymer chains, which do not attain a high degree of alignment/orientation crystallize epitaxially on the fibrils forming chain-folded structures.

Thus, crystallization after long-term shear is a multi-step sequential process. One possible scheme of sequential steps is described below. The first step is the ordering of a number of long, elongated and adjacent chains (with reduced kinetic hindrance and consequently low free energy) oriented parallel to the flow direction ('intermolecular' crystallization).

The 'bundles' of adjacent chains form fibrillar crystals, which serve as nuclei for crystallization of shorter relaxed chains. Thus, at the second step chain-folded oriented lamellae are growing over the 'primary linear nuclei' from the amorphous phase; lamellae are growing perpendicular to the flow direction, which was confirmed by time-resolved SAXS and WAXD studies of shear-induced iPP crystallization [45]. On a higher supermolecular level, these oriented lamellae growing over fibrils form threads. Thus, lamellae grow radially inside each thread. Evolving threads are parallel to the flow direction, since we observe it visually in the polarizing microscope (Fig. 9). The thickness of arising threads, when they become visible in the microscope, is of about 1 μm and higher (Fig. 9). This large diameter of evolving threads suggests that they exceed the dimensions of shish (fibrils) in shish–kebab's morphology, which was reported to be in the range of 30–100 nm for polyethylene in extensional flows [1]. The fact that large diameter of threads exceeds the typical value of central shish diameter does not mean that shish–kebab morphology is not existing in observed threads. As it was pointed out by Keller [1], there are micro- and macro-shish–kebabs. The latter are mostly too thick and hence opaque for direct TEM studies. Moreover, the distinction between macro- and micro-shish–kebabs leaves uncertainty as regards the nature of the objects in question in specific paper. The dimensions of our threads are similar to macro-shish–kebabs (with thick diameter on the order of microns), observed by polarizing microscopy in a polypropylene film formed after the melt was sheared by pressing [50]. Thus, our threads most likely consist of 'kebabs' grown over 'shish'. At even later times (third step), chain-folded lamellae with spherulitic morphologies are formed from the amorphous residual melt of even shorter chains with increased kinetic hindrance and higher free energy ('intramolecular' crystallization). Spherulites are directly observed on the micrographs at later stages of crystallization (Fig. 9). The latter consist of β-form crystals (which grow at late stages of crystallization over α-crystals), which is confirmed by direct X-ray studies of the processed samples [51].

The unanswered question is what governs the volume density of threads and their growth? Intuitively, it is clear that molecular parameters (molecular weight, molecular weight distribution, composition) and flow history (shear rate, total stress and strain) are responsible for the formation of threads. Also, spacial hindrance from arising threads or from the growth of spherulites between the threads may prevent the formation of the new threads. More work should be done to clarify this.

Thus, evolution of the optical properties follows the crystallization process starting from the typical melt behavior till fully crystallized solid state. This allows to probe different regimes of crystallization: nucleation, gelation, gross crystallization and overall crystallization kinetics. Scattering and transmittance data from rheo-optical apparatus, complemented by microscopy and rheology provides an important and diverse information for understanding the structure/property relationship during crystallization and other processes for various polymer systems.

4. Conclusions

Quiescent crystallization of iPP occurs in the typical spherulitic morphology. All spherulites are nucleated at about the same time and grow at equal rate, which results in a narrow size distribution. The gel point is reached before the spherulites actually touch each other which means that interaction between spherulites is effective through the amorphous phase. The crystallinity (from DSC) at the gel point is still low, however, it is large enough to give a substantial increase in the Q_δ-invariant. Further experiments are underway to see whether this is a more general phenomenon.

Shear flow induces anisotropic molecular conformations, preferably in the high molecular weight component of the iPP sample. The resulting orientation fluctuations (of highly oriented long chains and less oriented short chains) cause (1) an increase in crystallization rate and (2) highly elongated structures (threads) which are visible in the optical microscope and in anisotropic SALS patterns. The threads grow in thickness until, at later stages, additional spherulites nucleate on the threads and grow, presumably from the short chains.

A set-up has been built to measure time-resolved light scattering and transmittance properties in different polarization modes during shear in one experimental run. The versatile design makes it possible to use the device for studying various transient polymer processes under thermal and flow stimulation, such as phase separation, liquid–solid transition, nematic isotropic transitions in liquid-crystalline polymers, etc.

Acknowledgements

We are thankful to Richard Stein and Benjamin Hsiao for stimulating discussions. The support under grant from ExxonMobil (Baytown, TX) and under the MRSEC program at the University of Massachusetts, Amherst, (NSF DMR 9809365) is gratefully acknowledged. HHW thanks the Von Humboldt Foundation for support.

References

[1] Keller A, Kolnaar HW. Flow induced orientation and structure formation. In: Meijer HEH, editor. Processing of polymers, vol. 18. New York: VCH, 1997. p. 189–268.
[2] Strobl G. Eur Phys J E: Soft Mater 2000;3(2):165–83.
[3] Lotz B. Eur Phys J E: Soft Mater 2000;3(2):185–94.
[4] Mutukumar M. Eur Phys J E: Soft Mater 2000;3(2):199–202.
[5] Schwittay C, Mours M, Winter HH. Faraday Discuss 1995;101:93–104.
[6] Pogodina NV, Winter HH. Macromolecules 1998;31:8164–72.

[7] Pogodina NV, Siddiquee SKS, van Egmond JW, Winter HH. Macromolecules 1999;32:1167–74.
[8] Monasse BJ. Mater Sci 1995;30:5002–12.
[9] Tribaut C, Monasse B, Haudin JM. Colloid Polym Sci 1996;274:197–208.
[10] Duplay C, Monasse B, Haudin J, Costa J. Polym Int 1999;48:320–6.
[11] Wassner E, Maier RD. Processing of XIII International Congress on Rheology, vol. 1, August 2000; Cambridge, UK. p. 183–5.
[12] Eder G, Janeschitz-Kriegl H, Liedauer S. Prog Polym Sci 1990;15:629–714.
[13] Liedauer S, Eder G, Janeschitz-Kriegl H, Yershow P, Geymayer W, Ingolic E. Int Polym Process 1993;8:236–50.
[14] Eder G, Janeschitz-Kriegl H. Cahn RW, Haasen P, Kramer EJ, editors. Mater Sci Technol 1997;18:269–342.
[15] Yershow P, Janeschitz-Kriegl H. Rheol Acta 1996;35:127–33.
[16] Yershow P, Janeschitz-Kriegl H. Int Polym Process 1997;12:72–77.
[17] Kumaraswamy G, Verma RK, Issaian AM, Wang P, Kornfield JA, Yeh F, Msiao BS. Abstracts of APS Meetings, vol. 44, N1, March 1999; Atlanta, GA. p. 1561 (Part II).
[18] Kornfield J, Kumaraswamy G, Wang P, Verma R, Yeh F, Hsiao B. Proceedings of the ACS, PMSE Division, Fall Meeting, August 1999; New Orleans, LA. p. 326–7.
[19] Kumaraswamy G, Verma R, Kornfield J. Rev Sci Instrum 1999;70:2097–104.
[20] Kumaraswamy G, Issaian A, Kornfield J. Macromolecules 1999;32:7537–47.
[21] Stein RS, Wilkes GL. Structure and properties of oriented polymers. London: Applied Science, 1975 (p. 57–149).
[22] Fuller GG, Ylitalo CM. Optical rheometry of polymer liquids, Polymer rheology and processing. London: Elsevier, 1990 (p. 157–76).
[23] van Egmond JW, Werner DE, Fuller GG. J Chem Phys 1992;96:7742–57.
[24] Hashimoto T, Takebe T, Suehiro S. Polym J 1986;18:123–30.
[25] Läuger J, Gronski W. Rheol Acta 1995;34:70–79.
[26] Schmidt G. Shear orientation of lyotropic liquid crystalline mesophases. PhD Thesis. Germany: University of Freiburg; 1998.
[27] Cloke VM, Higgins JS, Phoon CL, Richardson SM, King SM, Done R, Cooper TE. Rev Sci Instrum 1996;67(9):3158–63.
[28] Thurston GB, Wilkinson RS. J Phys E: Sci Instrum 1973;6:289–93.
[29] Fuller GG. Annu Rev Fluid Mech 1990;22:387–417.
[30] Holly EE, Venkataraman S, Chambon F, Winter HH. J Non-Newt Fluid Mech 1988;27:17.
[31] Baumgaertel N, Winter HH. Rheol Acta 1989;28:511.
[32] Picot C, Stein RS. J Polym Sci, A-2 1970;8:1491–502.
[33] Hashimoto T, Ebisu S, Kawai H. J Polym Sci, Polym Lett Ed 1980;18:569–76.
[34] Stein RS, Rhodes MB. J Appl Phys 1960;31:1873.
[35] Stein RS, Wilson PR. J Appl Phys 1962;33:1914.
[36] Stein RS. Optical behavior of polymer blends. In: Paul DR, Newman S, editors. Polymer blends, vol. 1. New York: Academic Press, 1978.
[37] Goldstein M, Michalek ER. J Appl Phys 1955;26:1450.
[38] Koberstein J, Russell TP, Stein RS. J Polym Sci, Polym Phys Ed 1979;17:1719.
[39] Akpalu Y, Kielhorn L, Hsiao BS, Stein RS, Russel TP, van Egmond J, Muthukumar M. Macromolecules 1999;32:765.
[40] Olley RH, Bassett DC. Polymer 1989;30:399.
[41] Pogodina NV, Winter HH, Srinivas S. J Polym Sci B 1999;37:3512.
[42] Horst RH, Winter HH. Macromolecules 2000;33:130–6.
[43] Judge JT, Stein RS. J Appl Phys 1961;32:2357–63.
[44] Janeschitz-Kriegl H, Ratajski E, Wippel H. Colloid Polym Sci 1999;277:217–26.
[45] Kumaraswamy G, Verma RK, Issaian AM, Wang P, Kornfield JA, Yeh F, Hsiao BS, Olley RH. Polymer 2000;41(25):8931–40.
[46] Okada T, Saito H, Inoue T. Macromolecules 1992;25:1908–11.
[47] Pennings AJ, Kiel AM. Kolloid ZZ Polym 1965;205:160.
[48] Pennings AJ, van der Mark JMAA, Booij HC. Kolloid ZZ Polym 1970;236:99.
[49] Pennings AJ. J Polym Sci, Polym Symp 1977;59:395.
[50] Grubb DT, Odell JA, Keller A. J Mater Sci 1975;10:1410.
[51] Hsiao B. Private communication; 2001.
[52] Gerard H, Birch JM. Introduction to matrix methods in optics. New York: Wiley, 1975.